Journal of Sound and Vibration 499 (2021) 115995

Contents lists available at ScienceDirect

Journal of Sound and Vibration

journal homepage: www.elsevier.com/locate/jsv

Acoustic modelling and analyses of geometrically complex systems with Micro-perforated panels ☆

Xiaoqi Zhang [a,b], Li Cheng [b,*], Yang Liu [b,c], Jingtao Du [c]

[a] School of Energy and Power Engineering, Wuhan University of Technology, Wuhan 430063, China
[b] Department of Mechanical Engineering, The Hong Kong Polytechnic University, Kowloon, Hong Kong, China
[c] College of Power and Energy Engineering, Harbin Engineering University, Harbin 150001, China

ARTICLE INFO

Article history:
Received 25 October 2020
Revised 15 January 2021
Accepted 30 January 2021
Available online 2 February 2021

Keywords:
Geometrically complex systems
Modelling method
Micro-perforated panels
Hybrid sound reduction
Optimization

ABSTRACT

Modeling of vibro/acoustic systems with embedded acoustic components of complex geometries is a challenging task. In particular, the presence of irregular-shaped acoustic modules, which are usually treated by finite element (FE) method, increases system complexities and makes the use of existing sub-structuring modeling techniques cumbersome. To tackle the problem, an efficient three-dimensional sub-structuring modeling method is proposed in this paper. As an important sub-structural module, a dedicated coordinate transformation technique is established to cope with polygon acoustic components. The embodiment of the technique into the existing sub-structuring framework avoids the use of conventional FE modules, thus increasing the flexibility and the efficiency of the simulation, conducive to system optimization. As an example, noise reduction in a duct, comprising a Micro-Perforated Panel (MPP) liner and a trapezoidal expansion chamber, is examined. The accuracy of the proposed model is firstly validated against both FE simulations and experiments. Numerical results uncover a dual hybrid sound reduction process, namely sound absorption of the MPP and wave reflection due to the geometry changes of the duct. Optimizations based on the proposed sub-structuring technique allow one to balance the hybrid reflective-absorptive effects through proper parameter tuning to maximize the sound attenuation within a prescribed frequency range.

1. Introduction

Vibro/acoustic systems with embedded acoustic components of complex geometries are commonly seen in engineering problems. A generic configuration is illustrated in Fig. 1, in which an irregular-shaped acoustic enclosure is nested with other types of vibro/acoustic elements. Application examples of such a configuration can be found in various noise control problems such as in room acoustics, vehicle cabin noise problems, duct noise and silencer design etc. The effective handling of such complex systems in terms of design, modelling and optimization is technically challenging.

This issue is investigated in the present work with a twofold objective, thus showing its novelty: 1) proposing an effective modeling technique based on coordinate transformation to deal with irregular-shaped acoustic components before its embodiment into a general sub-structuring modelling framework; and 2) as a typical application example, exploring the

☆ Handling editor: O Guasch.

* Corresponding author.
E-mail address: li.cheng@polyu.edu.hk (L. Cheng).

https://doi.org/10.1016/j.jsv.2021.115995
0022-460X/

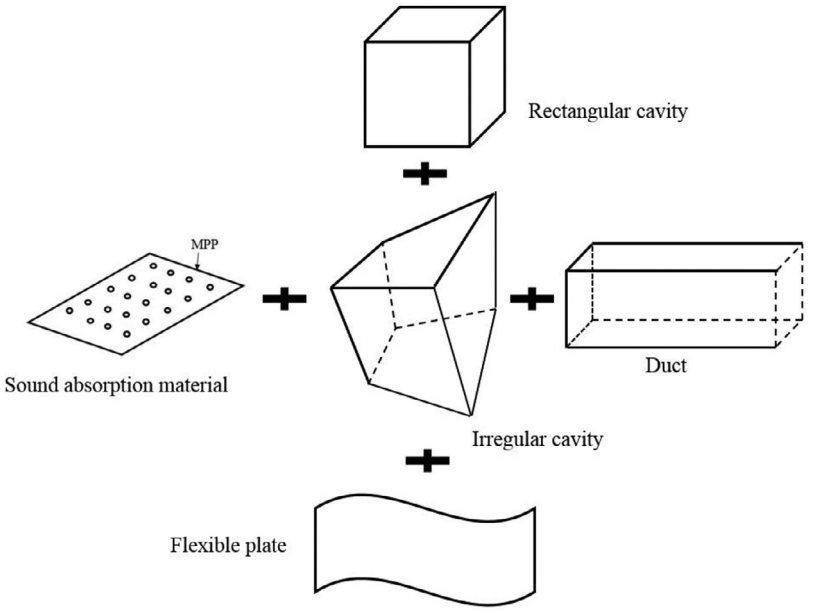

Fig. 1. Sketch of a typical vibro-acoustic system involving various vibro/acoustic and control elements, some with irregular shapes.

design, optimization as well as the underlying physical mechanisms of an acoustic duct comprising Micro-perforated panel (MPP) liners and irregular-shaped expansion chambers for noise control applications.

MPPs, made of fibrous-free, incombustible and cleanable materials, are recognized as one of the promising next generation sound absorption materials. With perforations in sub-millimeter range, the panels can provide high acoustic resistance and low acoustic reactance upon a proper sizing to achieve broadband noise absorptions without the use of porous materials. Due to their appealing features, MPPs show promise for noise control applications in numerous engineering products. Since the pioneer work of Maa [1,2], MPPs have been widely used as sound absorbers in applications such as building acoustics [3–5], environmental noise abatement [6,7] as well as noise control in compact mechanical systems [8–11].

More specific to duct noise control, most of existing MPP-related research focus on straight ducts involving rather simple system geometry [12–16]. However, it can be surmised that, when MPPs are put into a duct with irregular shaped expansion chamber, sound reflections can be expected as a result of the impedance mismatch due to the cross-sectional changes along the duct. This effect, if properly utilized, may add to the well-known sound absorption by the MPPs, thus offering an increased design room to maximize the sound attenuation, since in addition to the conventional tuning of the MPP parameters in a straight duct [12], other system parameters like the shape of the cavity can also be considered. This, however, poses harsh requirements on the simulation and optimization tools, in particular, with the presence of irregular shaped expansion chambers.

In a broader sense, the need of dealing with complex system with irregular-shaped acoustic cavities is not specific and limited to duct noise problems. While simple geometries can be readily treated analytically [9,17,18], Finite Element Method (FEM) still remains the most commonly used approach to deal with complex-shaped cavities. As alternatives, effort to develop more physical and presumably more flexible methods has been persistent. In fact, when used as a separate system, irregular-shaped acoustic cavities have been the subject of study in the open literature [19–25]. Existing techniques root in the idea that the acoustic pressure inside an irregular-shaped cavity can be expressed as the normal expansion of rigid-walled modes of the rectangular cavity englobing the irregular volume. Based on the idea, sound fields in various irregular enclosures have been investigated, exemplified by the prediction of resonance frequencies [19], decay time of acoustic modes [23] and sound pressure distributions or mode shapes in enclosures [25]. However, the drawback of these approaches lies in that approximating the cavity geometry by regular shapes introduces inevitable computational errors. Meanwhile, when the geometrical irregularity of the cavity increases, a refined discretization into a series of sub-cavities is required [19], thus increasing the computational cost. Re-examining the issue from a system viewpoint, when an irregular-shaped cavity is present as a component in a vibro/acoustic system, other considerations like calculation efficiency, the need for flexible parameter tuning and optimization are some other additional factors which make the task even more challenging.

As efficient means to model a complex vibro/acoustic system, methods based on sub-structuring principle have been attracting persistent attention and covering wide range of various topics involving structural displacement representation [26], structural vibration analyses [27], acoustic [28] and vibro-acoustic modelling [29] etc. Typical sub-structuring approaches segment the whole system into several subsystems, which are *a prior* characterized before assembling them together through different physical quantities such as impedance or mobility [29], transfer matrix [30] and more recently, the

Patch Transfer Functions (PTFs) [9,11,12,17,18,31]. Research has demonstrated the efficacy of the method in terms of system modelling and optimization when sub-systems take simple geometries in the optimization loop [11,12,17,31]. Existing PTF modelling framework requires the irregular-shaped acoustic components be treated by FEM, which is acceptable for a given system configuration, but becomes problematic for system optimization in which the shape itself undergoes changes during the optimization iteration. Therefore, the presence of the irregular cavity poses tremendous difficulties to the existing sub-structuring techniques.

Motivated by this, this paper proposes a technique based on coordinate transformation to deal with the modelling of irregular cavity subsystems, before being embedded into the general PTF framework. Coordinate transformation is widely used in 3D FEM when evaluating element contributions in the mass or stiffness matrix via a Jacobian from a reference element parametrized by coordinates varying within a cubic domain. Enlightened by this, this technique is cast to fit into the current PTF framework to cope with geometry changes of subsystems during the system modelling and optimization. With this treatment, an irregular-shaped polygon cavity can be transformed into a regular rectangular one in a different coordinate system [32] so that the physical quantities required by the PTF method can be analytically obtained. This is then packaged as a subsystem module to be embedded into the general PTF framework. As such, the whole solution package proposed is expected to improve the efficiency of sub-structuring method in terms of handling complex systems, conducive to system optimization.

In what follows, the principle of the coordinate transformation technique along with the PTF approach are first illustrated in Section 2 using a representative duct configuration. The proposed method is then validated against FEM simulations and experimental results in Section 3. Numerical analyses are performed to investigate the silencing performance of a duct with a MPP liner and an irregular-shaped expansion chamber in Section 4. With a particular focus on the cavity shape-induced wave reflection and its joint effect with the MPP-induced sound absorption, underlying mechanisms underpinning the observed noise reduction are exploited, and the necessity for system parameter tuning and eventually system optimization to achieve desired silencing performance is demonstrated. Subsequently, two optimization examples are given to demonstrate the capability and the computational efficiency of the proposed modelling approach, and the enhanced duct noise mitigation within prescribed frequency ranges.

2. Numerical method

2.1. Model and PTF approach

The sub-structuring PTF approach, to be employed to simulate the acoustic field of a complex system, is first illustrated. A representative configuration, shown in Fig. 2, is considered here. The system comprises a MPP liner and an irregular-shaped expansion chamber in an infinitely long acoustic duct. The MPP liner is flush-mounted on one of the inner wall surfaces of the duct.

The global system is firstly segmented into several decoupled subsystems, alongside the generation of coupling interfaces between each pair of adjacent subsystems. In the present case, the whole system is partitioned into six subsystems as illustrated in Fig. 3: a semi-infinite inlet duct, MPP and its backing cavity, the main cavity above the MPP liner, a trapezoidal sub-cavity and a semi-infinite outlet duct. Four coupling interfaces are then formed, donated by C1, C2, C3 and C4, respectively. These four interfaces are segmented into several elements, called patches. The required number of patches to ensure the calculation convergence up to a given frequency in the PTF approach is well-established in previous studies, namely the patch size should be smaller than the half minimum acoustic wavelength of interest [9,18]. According to this half-wavelength criterion [9,18] the total segmented patch number for four interfaces are N_1, N_2, N_3 and N_4, respectively. Each subsystem needs to be *a priori* characterized separately, by the so-called transfer functions between different patches, called patch transfer functions (PTFs), which are defined as the ratio of the average response at a receiving patch to an excitation at another patch. For vibrating structure and an acoustic cavity, the patch mobility Y_{re} and patch impedance Z_{re}

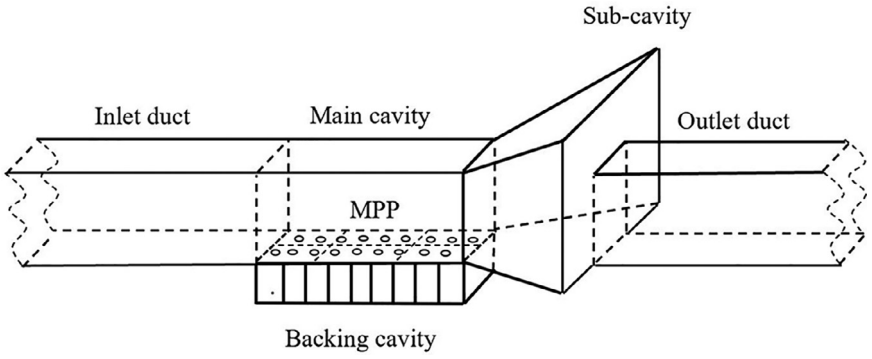

Fig. 2. Sketch of the duct noise problem involving a MPP liner and trapezoidal expansion chamber.

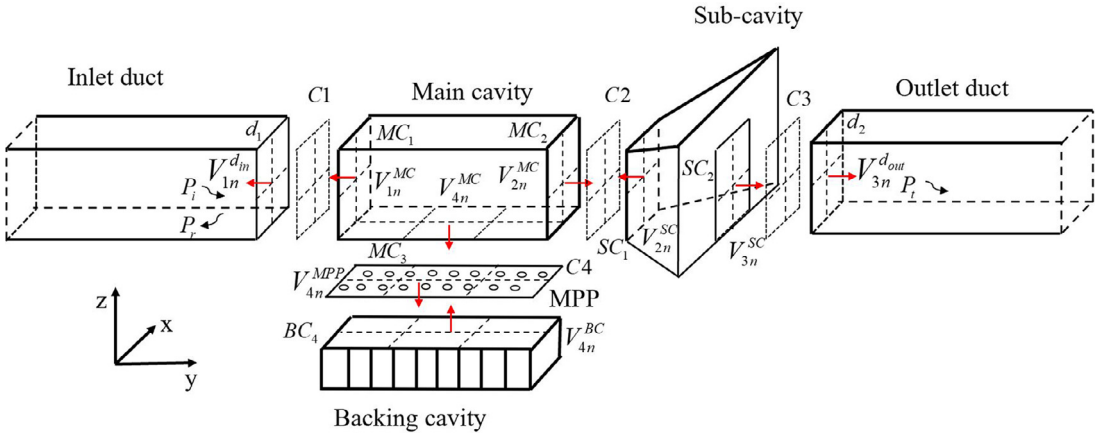

Fig. 3. Sub-structure treatment of the duct system.

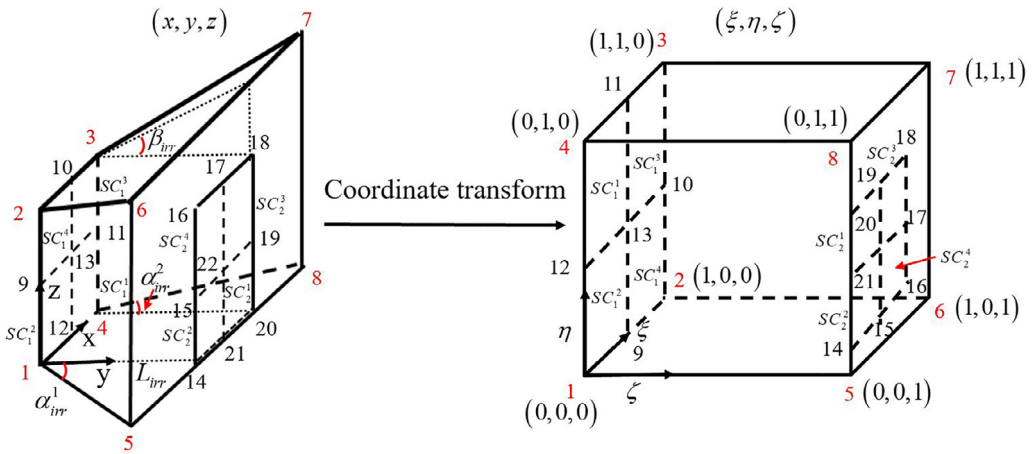

Fig. 4. Illustration of coordinate transformation technique.

are used as PTFs, respectively as

$$Y_{\mathrm{re}} = \frac{\bar{u}_r}{\bar{f}_e}, \tag{1}$$

$$Z_{\mathrm{re}} = \frac{\bar{p}_r}{\bar{u}_e}. \tag{2}$$

The mean normal velocity $\bar{u}_r = \frac{1}{S_r}\int_{S_r} u_{x,y,z}dS$ and the mean acoustic pressure $\bar{p}_r = \frac{1}{S_r}\int_{S_r} p_{x,y,z}dS$ are, respectively, the average response at a receiving patch resulted from a mean normal force excitation $\bar{f}_e = \frac{1}{S_e}\int_{S_e} f_{x,y,z}dS$ or a mean normal velocity $\bar{u}_e = \frac{1}{S_e}\int_{S_e} u_{x,y,z}dS$ exerted on an excited patch e in structural or acoustic domain, in which S_r and S_e are the surface area of the receiving and excited patches, respectively. Before considering the coupling, the PTFs of each uncoupled subsystem are separately calculated.

Both the main cavity in the duct and the backing cavity behind the MPP can be modeled as a 3D rectangular cavity, allowing for analytical treatment [12]. The inlet and the outlet duct can be treated as semi-infinite ducts with no sound reflection from the termination, which can also be readily handled [12,17]. The vibration of the MPP, though can be incorporated into the model, is ignored for simplicity.

As to the trapezoidal sub-cavity, FEM could be used for its PTF calculation. This comes with all the inconveniences discussed in the Introduction. The following section proposes an alternative to deal with this acoustic module involving irregular geometrical shape.

2.2. Modelling irregular cavity with coordinate transformation

The trapezoidal cavity, described in the physical Cartesian x-y-z coordinate system shown in Fig. 4, can be mapped into a regular rectangular cavity with unit length in a different coordinate system ξ-η-ζ by performing a coordinate transfor-

mation. After transformation, the PTF calculations of the irregular cavity with inclined walls can be analytically performed since the geometry of the transformed cavity will have a regular and simple shape.

The mapping relationship between these two coordinate systems is determined by the location relationship of eight vertexes (x_i, y_i, z_i) of the trapezoidal cavity as:

$$\begin{aligned} x &= N_1x_1 + N_2x_2 + N_3x_3 + N_4x_4 + N_5x_5 + N_6x_6 + N_7x_7 + N_8x_8, \\ y &= N_1y_1 + N_2y_2 + N_3y_3 + N_4y_4 + N_5y_5 + N_6y_6 + N_7y_7 + N_8y_8, \\ z &= N_1z_1 + N_2z_2 + N_3z_3 + N_4z_4 + N_5z_5 + N_6z_6 + N_7z_7 + N_8z_8, \end{aligned} \tag{3}$$

where

$$\begin{aligned} &N_1 = (1-\xi)(1-\eta)(1-\zeta),\ N_2 = \xi(1-\eta)(1-\zeta), \\ &N_3 = \xi\eta(1-\zeta),\ N_4 = (1-\xi)\eta(1-\zeta), \\ &N_5 = (1-\xi)(1-\eta)\zeta,\ N_6 = \xi(1-\eta)\zeta, \\ &N_7 = \xi\eta\zeta,\ N_8 = (1-\xi)\eta\zeta. \end{aligned} \tag{4}$$

Based on Eqs. (3) and (4), the relationship between the first spatial derivative with respect to x, y, z and ξ, η, ζ can be expressed as follows

$$\begin{Bmatrix} \frac{\partial()}{\partial\xi} \\ \frac{\partial()}{\partial\eta} \\ \frac{\partial()}{\partial\zeta} \end{Bmatrix} = \begin{bmatrix} \frac{\partial x}{\partial\xi} & \frac{\partial y}{\partial\xi} & \frac{\partial z}{\partial\xi} \\ \frac{\partial x}{\partial\eta} & \frac{\partial y}{\partial\eta} & \frac{\partial z}{\partial\eta} \\ \frac{\partial x}{\partial\zeta} & \frac{\partial y}{\partial\zeta} & \frac{\partial z}{\partial\zeta} \end{bmatrix} \begin{Bmatrix} \frac{\partial()}{\partial x} \\ \frac{\partial()}{\partial y} \\ \frac{\partial()}{\partial z} \end{Bmatrix} = \mathbf{J} \begin{Bmatrix} \frac{\partial()}{\partial x} \\ \frac{\partial()}{\partial y} \\ \frac{\partial()}{\partial z} \end{Bmatrix}, \tag{5}$$

where $\mathbf{J}$ is the Jacobian matrix.

The sound pressure in the rigid-walled irregular cavity $p_{\mathrm{irr}}(x, y, z)$, is expressed as the summation of a series of cosine functions, expressed in terms of their corresponding locations in the transformed rigid-walled regular cavity as

$$p_{\mathrm{irr}}(x, y, z) = p_{\mathrm{irr}}(\xi, \eta, \zeta) = \sum_{m_\xi=0}^{N_\xi} \sum_{m_\eta=0}^{N_\eta} \sum_{m_\zeta=0}^{N_\zeta} \phi_{m_\xi m_\eta m_\zeta} \cos(m_\xi \pi \xi) \cos(m_\eta \pi \eta) \cos(m_\zeta \pi \zeta), \tag{6}$$

where $\phi_{m_\xi m_\eta m_\zeta}$ is a set of unknown coefficients, to be determined based on the energy principle. To this end, the total potential energy U_{irr} and kinetic energy T_{irr} of the trapezoidal cavity write

$$U_{\mathrm{irr}} = \frac{1}{2\rho c^2} \int_V p_{\mathrm{irr}}^2(x, y, z) dV = \frac{1}{2\rho c^2} \int_0^1 \int_0^1 \int_0^1 p_{\mathrm{irr}}^2(\xi, \eta, \zeta) |\mathbf{J}| d\xi d\eta d\zeta, \tag{7}$$

and

$$\begin{aligned} T_{\mathrm{irr}} &= \frac{1}{2\rho\omega^2} \int_V \left(\frac{\partial p_{\mathrm{irr}}(x,y,z)}{\partial x} \right)^2 + \left(\frac{\partial p_{\mathrm{irr}}(x,y,z)}{\partial y} \right)^2 + \left(\frac{\partial p_{\mathrm{irr}}(x,y,z)}{\partial z} \right)^2 dV \\ &= \frac{1}{2\rho\omega^2} \int_0^1 \int_0^1 \int_0^1 \left[\begin{array}{l} \left(\left[\mathbf{J}^{-1}\right]_{11} \frac{\partial p_{\mathrm{irr}}(\xi,\eta,\zeta)}{\partial\xi} + \left[\mathbf{J}^{-1}\right]_{12} \frac{\partial p_{\mathrm{irr}}(\xi,\eta,\zeta)}{\partial\eta} + \left[\mathbf{J}^{-1}\right]_{13} \frac{\partial p_{\mathrm{irr}}(\xi,\eta,\zeta)}{\partial\zeta} \right)^2 \\ + \left(\left[\mathbf{J}^{-1}\right]_{21} \frac{\partial p_{\mathrm{irr}}(\xi,\eta,\zeta)}{\partial\xi} + \left[\mathbf{J}^{-1}\right]_{22} \frac{\partial p_{\mathrm{irr}}(\xi,\eta,\zeta)}{\partial\eta} + \left[\mathbf{J}^{-1}\right]_{23} \frac{\partial p_{\mathrm{irr}}(\xi,\eta,\zeta)}{\partial\zeta} \right)^2 \\ + \left(\left[\mathbf{J}^{-1}\right]_{31} \frac{\partial p_{\mathrm{irr}}(\xi,\eta,\zeta)}{\partial\xi} + \left[\mathbf{J}^{-1}\right]_{32} \frac{\partial p_{\mathrm{irr}}(\xi,\eta,\zeta)}{\partial\eta} + \left[\mathbf{J}^{-1}\right]_{33} \frac{\partial p_{\mathrm{irr}}(\xi,\eta,\zeta)}{\partial\zeta} \right)^2 \end{array} \right] |\mathbf{J}| d\xi d\eta d\zeta \end{aligned} \tag{8}$$

where ρ is the air density; c is the sound speed; ω is the angular frequency; $\mathbf{J}^{-1}$ is the inverse of Jacobian matrix $\mathbf{J}$, and $[\mathbf{J}^{-1}]_{ij}$ is the element (i, j) in matrix $\mathbf{J}^{-1}$.

Note that Eq. (6) only applies to a cavity with acoustically-rigid walls, which is exactly what is needed by the definition of the patch transfer functions of a sub-cavity before it is coupled to the rest of the system.

The work done by one excitation patch on the boundary surface of the trapezoidal cavity, like the patch on the interface where $y = 0$ shown in Fig. 4, excited with a uniformly distributed unit displacement writes

$$W_e = \int_{x_1^e}^{x_2^e} \int_{z_1^e}^{z_2^e} p_{\mathrm{irr}}(x, 0, z) dx dz = \int_{\xi_1^e}^{\xi_2^e} \int_{\eta_1^e}^{\eta_2^e} p_{\mathrm{irr}}(\xi, \eta, 0) |\mathbf{J}_{2\times2}| d\xi d\eta, \quad \forall e \in [1, \ldots, N_2], \tag{9}$$

where $\mathbf{J}_{2\times2} = \begin{bmatrix} \frac{\partial x}{\partial\xi} & \frac{\partial z}{\partial\xi} \\ \frac{\partial x}{\partial\eta} & \frac{\partial z}{\partial\eta} \end{bmatrix}$.

Writing Lagrangian for the trapezoidal acoustical cavity

$$L = U_{\mathrm{irr}} - T_{\mathrm{irr}} - W_e, \tag{10}$$

and applying Lagrange equation with respect to all the unknown coefficients yield the following condensed matrix form:

$$\left(\mathbf{M}_{\mathrm{irr}} - \frac{\mathbf{K}_{\mathrm{irr}}}{\omega^2} \right) \boldsymbol{\phi} = \mathbf{W}, \tag{11}$$

where $\mathbf{M_{irr}}$ and $\mathbf{K_{irr}}$ can be interpreted as the mass and stiffness matrices of the irregular cavity with rigid walls, $\boldsymbol{\phi}$ is a vector containing the unknown coefficients and $\mathbf{W}$ is the external work vector done by one excitation patch of the trapezoidal cavity.

Solving Eq. (11) gives the unknown coefficient $\phi_{m_\xi m_\eta m_\zeta}$, which allows the calculation of the sound pressure field in the irregular cavity through Eq. (6).

Finally, according to Eq. (2), the PTF between patches in the irregular cavity, for example, when the receiving patch is on the interface where $y = 0$ shown in Fig. 4, can be obtained as

$$Z_{\mathrm{re}}^{\mathrm{irr}} = \frac{\bar{p}_{\mathrm{irr}}^{r}}{\bar{u}_{\mathrm{irr}}^{e}} = \frac{\bar{p}_{\mathrm{irr}}^{r}}{\mathrm{j}\omega} = \frac{\int_{\xi_1^r}^{\xi_2^r}\int_{\eta_1^r}^{\eta_2^r} p_{\mathrm{irr}}(\xi,\eta,0)\,d\xi\,d\eta}{\mathrm{j}\omega S_{\mathrm{rec}}^{r}}, \tag{12}$$

where S_{rec}^{r} is the surface area of one receiving patch in the transformed rectangular cavity.

Note that the above formulations apply to a trapezoidal cavity with eight vertices. However, the proposed framework can be extended to other irregular-shaped polygonal cavities formed by polygons. For more complex cases such as concave, convex boundaries, Eqs. (3) and (4) should be rederived with the consideration of more vertices which will impact on the transformation of their positions.

2.3. Global system response and acoustic metrics calculations

After obtaining the PTFs of all separated subsystems, by using the linear superposition principle and applying the continuity condition on the connecting patches of the four coupling surfaces, namely the force balance of each patch and the equality of the normal velocity, subsystems are finally coupled together to yield:

$$\begin{aligned}
&\mathbf{P}^{\sim\mathbf{d_1}} + \mathbf{Z}^{\mathbf{d_1}}\mathbf{V}_{\mathbf{1n}}^{\mathbf{d_1}} = \mathbf{Z}_{\mathbf{11}}^{\mathbf{MC}}\mathbf{V}_{\mathbf{1n}}^{\mathbf{MC}} + \mathbf{Z}_{\mathbf{12}}^{\mathbf{MC}}\mathbf{V}_{\mathbf{2n}}^{\mathbf{MC}} + \mathbf{Z}_{\mathbf{13}}^{\mathbf{MC}}\mathbf{V}_{\mathbf{4n}}^{\mathbf{MC}},\\
&\mathbf{Z}_{\mathbf{11}}^{\mathbf{SC}}\mathbf{V}_{\mathbf{2n}}^{\mathbf{SC}} + \mathbf{Z}_{\mathbf{12}}^{\mathbf{SC}}\mathbf{V}_{\mathbf{3n}}^{\mathbf{SC}} = \mathbf{Z}_{\mathbf{21}}^{\mathbf{MC}}\mathbf{V}_{\mathbf{1n}}^{\mathbf{MC}} + \mathbf{Z}_{\mathbf{22}}^{\mathbf{MC}}\mathbf{V}_{\mathbf{2n}}^{\mathbf{MC}} + \mathbf{Z}_{\mathbf{23}}^{\mathbf{MC}}\mathbf{V}_{\mathbf{4n}}^{\mathbf{MC}},\\
&\mathbf{Z}_{\mathbf{21}}^{\mathbf{SC}}\mathbf{V}_{\mathbf{2n}}^{\mathbf{SC}} + \mathbf{Z}_{\mathbf{22}}^{\mathbf{SC}}\mathbf{V}_{\mathbf{3n}}^{\mathbf{SC}} = \mathbf{Z}^{\mathbf{d_2}}\mathbf{V}_{\mathbf{3n}}^{\mathbf{d_2}},\\
&\mathbf{Y}(\mathbf{Z}_{\mathbf{31}}^{\mathbf{MC}}\mathbf{V}_{\mathbf{1n}}^{\mathbf{MC}} + \mathbf{Z}_{\mathbf{32}}^{\mathbf{MC}}\mathbf{V}_{\mathbf{2n}}^{\mathbf{MC}} + \mathbf{Z}_{\mathbf{33}}^{\mathbf{MC}}\mathbf{V}_{\mathbf{4n}}^{\mathbf{MC}} - \mathbf{Z}_{\mathbf{44}}^{\mathbf{BC}}\mathbf{V}_{\mathbf{4n}}^{\mathbf{BC}}) = \mathbf{V}_{\mathbf{4n}}^{\mathbf{MPP}},\\
&\mathbf{V}_{\mathbf{1n}}^{\mathbf{MC}} = \mathbf{V}_{\mathbf{1n}}^{\mathbf{d1}},\\
&\mathbf{V}_{\mathbf{2n}}^{\mathbf{MC}} = \mathbf{V}_{\mathbf{2n}}^{\mathbf{SC}},\\
&\mathbf{V}_{\mathbf{3n}}^{\mathbf{d_2}} = \mathbf{V}_{\mathbf{3n}}^{\mathbf{MC}},\\
&\mathbf{V}_{\mathbf{4n}}^{\mathbf{MC}} = \mathbf{V}_{\mathbf{4n}}^{\mathbf{MPP}} = -\mathbf{V}_{\mathbf{4n}}^{\mathbf{BC}}.
\end{aligned} \tag{13}$$

where $\mathbf{Z_{ij}}$ is the $N_i \times N_j$ cavity impedance matrix, $\mathbf{Y}$ the $N_4 \times N_4$ panel mobility matrix, $\mathbf{Z^{d_1}}$ the $N_1 \times N_1$ inlet duct impedance matrix, $\mathbf{Z^{d_2}}$ the $N_3 \times N_3$ outlet duct impedance matrix, $\mathbf{P^{\sim d_1}}$ the $N_1 \times 1$ external pressure excitation vector, $\mathbf{V_{in}}$ the $N_i \times 1$ normal velocity vector.

Eq. (13) can be further condensed into the following form as,

$$\{\mathbf{Z}\}\{\mathbf{V}\} = \{\mathbf{F}\}, \tag{14}$$

where $\mathbf{Z} = \begin{bmatrix} \mathbf{Z}_{\mathbf{11}}^{\mathbf{MC}} - \mathbf{Z}^{\mathbf{d_1}} & \mathbf{Z}_{\mathbf{12}}^{\mathbf{MC}} & \mathbf{0} & \mathbf{Z}_{\mathbf{13}}^{\mathbf{MC}} \\ \mathbf{Z}_{\mathbf{21}}^{\mathbf{MC}} & \mathbf{Z}_{\mathbf{22}}^{\mathbf{MC}} - \mathbf{Z}_{\mathbf{11}}^{\mathbf{SC}} & -\mathbf{Z}_{\mathbf{12}}^{\mathbf{SC}} & \mathbf{Z}_{\mathbf{23}}^{\mathbf{MC}} \\ \mathbf{0} & \mathbf{Z}_{\mathbf{21}}^{\mathbf{SC}} & \mathbf{Z}_{\mathbf{22}}^{\mathbf{SC}} - \mathbf{Z}^{\mathbf{d_2}} & \mathbf{0} \\ \mathbf{YZ}_{\mathbf{31}}^{\mathbf{MC}} & \mathbf{YZ}_{\mathbf{32}}^{\mathbf{MC}} & \mathbf{0} & \mathbf{Y}(\mathbf{Z}_{\mathbf{33}}^{\mathbf{MC}} + \mathbf{Z}_{\mathbf{44}}^{\mathbf{BC}}) - \mathbf{I} \end{bmatrix}$,

$\mathbf{V} = \begin{bmatrix} \mathbf{V}_{\mathbf{1n}}^{\mathbf{MC}} \\ \mathbf{V}_{\mathbf{2n}}^{\mathbf{MC}} \\ \mathbf{V}_{\mathbf{3n}}^{\mathbf{d_2}} \\ \mathbf{V}_{\mathbf{4n}}^{\mathbf{MC}} \end{bmatrix}$ and $\mathbf{F} = \begin{bmatrix} \mathbf{P}^{\sim\mathbf{d_1}} \\ \mathbf{0} \\ \mathbf{0} \\ \mathbf{0} \end{bmatrix}$.

If the backing cavity is to be partitioned into smaller cavities, as shown in Fig. 3, it can be regarded as a combination of multiple unit cells, each comprising a MPP facing and an acoustic backing cavity. Assuming the unit cells are well separated from each other by solid partition walls, the mobility matrix $\mathbf{Y}$ of the coupling surface C4 and the backing cavity impedance matrix $\mathbf{Z}_{\mathbf{44}}^{\mathbf{BC}}$ can be constructed by combining all the unit cells as a common subsystem as detailed in Ref [12].

Upon solving Eq. (14), the mean pressure and normal velocity of all patches in each subsystem can then be obtained; different acoustic metrics of the entire system can then be obtained using the calculated patch responses. The TL (Transmission Loss), sound absorption coefficient and reflection coefficient calculations of the system are used for analyses. TL is defined as

$$\mathrm{TL} = 10\log_{10}\frac{\prod_{\mathrm{in}}}{\prod_{\mathrm{out}}}, \tag{15}$$

where,

$$\prod_{\mathrm{in}} = \frac{|p_i|^2}{2\rho c} S_1, \tag{16}$$

$$\prod_{\text{out}} = \frac{1}{2}\int_{S_3} \text{Re}\{P_3 V_3^*\} dS_3, \tag{17}$$

are the incident and transmitted sound power, respectively; $|p_i|$ is the amplitude of the incidence acoustic wave; V_3 and P_3 are the normal velocity and the sound pressure at interface 3; S_1 and S_3 are the total surface area of interface 1 and 3; the superscript * represents the complex conjugate.

The sound reflection coefficient R is defined as

$$R = \frac{\prod_r}{\prod_{\text{in}}} = \frac{\prod_{\text{in}} - \prod_t^1}{\prod_{\text{in}}}, \tag{18}$$

where, $\prod_r$ and $\prod_t^1$ are the reflected and transmitted sound power at interface 1, respectively.

$$\prod_t^1 = \frac{1}{2}\int_{S_1} \text{Re}\{P_1 V_1^*\} dS, \tag{19}$$

in which V_1 and P_1 are the normal velocity and the sound pressure at the interface 1.

The sound absorption coefficient α is defined as the fraction of the sound power absorbed by the MPP absorber when an incidence plane wave is transmitted through the whole system, which expressed as

$$\alpha = \frac{\prod_t^1 - \prod_{\text{out}}}{\prod_{\text{in}}}. \tag{20}$$

3. Experimental validation

Experiments are conducted to validate the proposed model using the test sample, as shown in Fig. 5. An aluminum MPP is placed on one inner surface of the duct with a width and a length of 100 and 500 mm, respectively. The perforation ratio of the MPP is 0.945%. The diameter of the MPP hole and thickness of the panel are both 0.5 mm. The depth of the backing cavity behind the MPP is 25 mm. The honeycomb structure thus consists of 2 × 15 (along the width and length directions, respectively) equally spaced cells, amounting to a total of 30 small rectangular cavities in the backing cavity behind the MPP. The MPP liner can be regarded as locally reacting. The dimension of the model is given by Fig. 5.

The experimental setup is sketched in Fig. 6. Measurements are conducted in a duct with a cross section of 100 × 100 mm and a cut-on frequency of 1700 Hz. The energy emitted by the speaker obviously varies with frequencies. However, during experiments, verifications were made to make sure that the energy at every measured single frequency was strong enough to ensure a reasonable signal-to-noise ratio. The TL is measured by using the four-microphone-two-source method [33]. Two of the four 1/4-inch. microphones are flush-mounted upstream the MPP portion and the two others in the downstream segment. The separation distance between each pair of microphones is 80mm. Fig. 7 shows a photo of the test set-up. The distance between the two microphones in a pair determines the effective frequency range for TL measurement. More specifically, one should ensure that $\frac{0.05c}{L_{\text{mic}}} \le f \le \frac{0.4c}{L_{\text{mic}}}$ for the four-microphone-two-source method, where L_{mic} is the distance between each pair of microphones [33].

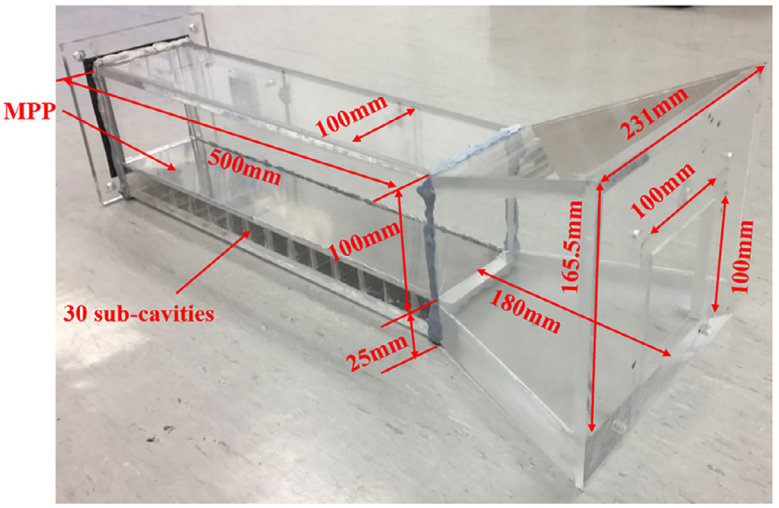

Fig. 5. Test sample.

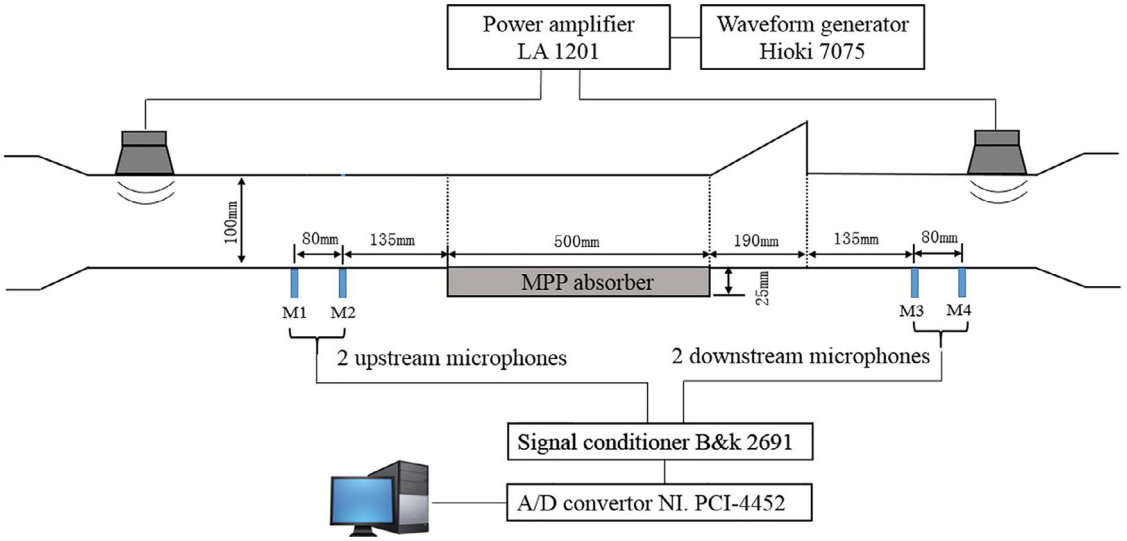

Fig. 6. Sketch of the experimental set-up.

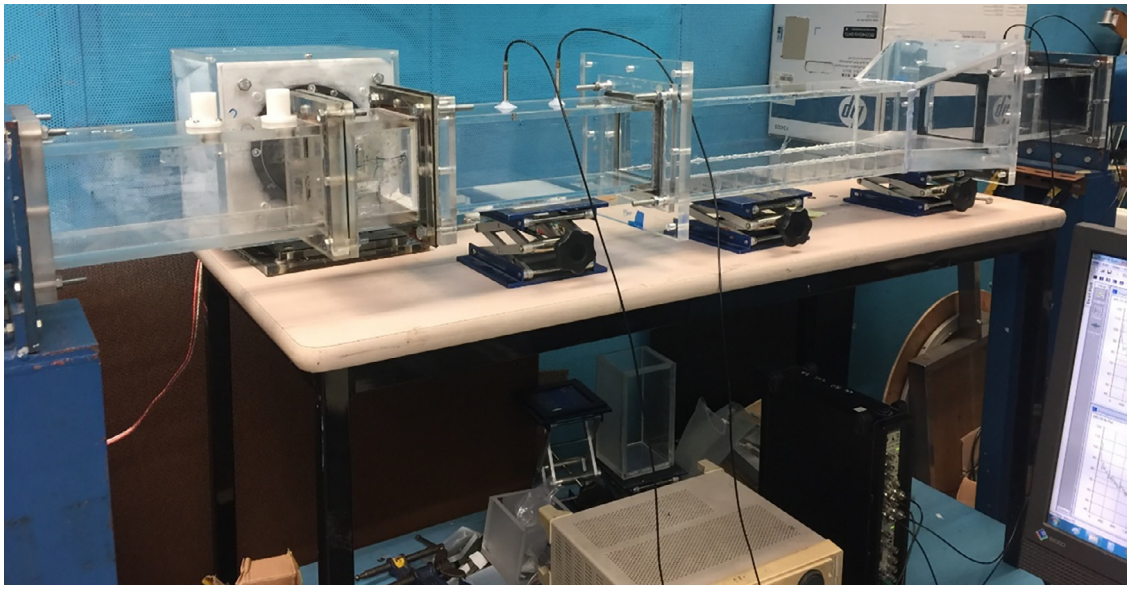

Fig. 7. Photo of the experimental setup.

The sound absorption coefficient α is derived from

$$\alpha = \frac{\prod_{\text{in}}^{\text{exp}} - \prod_{\text{out}}^{\text{exp}} - \prod_{\text{r}}^{\text{exp}}}{\prod_{\text{in}}^{\text{exp}}}, \tag{21}$$

where

$$\prod_{\text{in}}^{\text{exp}} = \frac{\left|p_i^{\text{exp}}\right|^2}{2\rho c} S_{\text{duct}}, \tag{22}$$

$$\prod_{r}^{\text{exp}} = \frac{\left|p_r^{\text{exp}}\right|^2}{2\rho c} S_{\text{duct}}, \tag{23}$$

are the measured incident and reflected sound power in the inlet duct, respectively. In Eqs. (22) and (23), S_{duct} is the cross-sectional area of the duct, $|p_i^{\text{exp}}|$ and $|p_r^{\text{exp}}|$ are the measured pressure amplitude of the incident and reflected waves

in the inlet part of the duct, which is obtained from two upstream microphones (M1 and M2 in Fig. 6) by using modal-decomposition method. $\prod_{\text{out}}^{\text{exp}}$ is the measured transmitted sound power, which is derived according to the definition of the TL as

$$\prod_{\text{out}}^{\text{exp}} = \frac{\prod_{\text{in}}^{\text{exp}}}{10^{\text{TL}/10}}. \tag{24}$$

The accuracy of the simulation model is validated through comparisons with measured data. The TL, sound absorption coefficient and reflection coefficient curves of the system ($d = t = 0.5$mm and $\delta = 0.954\%$) without flow are compared in Fig. 8. FEM results are also shown for further validation. A three-dimensional FEM model is built for validation purposes using COMSOL. Plane wave radiation is imposed on both the inlet and the outlet ends of the duct to mimic no reflection boundary conditions. The enclosed acoustic domain is discretized in such a way that at least 6 elements are used per wavelength. Verifications made confirmed that the meshing was sufficiently dense to ensure the simulation accuracy within the frequency range of interest considered in this paper.

Three peaks at $f = 979$Hz, $f = 1169$Hz and $f = 1625$Hz can be seen on the TL curve from Fig. 8a. While the first two peaks are actually generated mainly by the absorption provided by the MPP liner, the one at $f = 1625$Hz is caused by both the MPP absorption and the reflection due to the impedance mismatch induced by the cross-sectional changes in the trapezoidal part of the duct. More detailed analyses on these TL peaks are presented in the next section. The comparisons show that while the predicted TL, absorption coefficient and reflection coefficient curves from the present model match perfectly with those from the FE simulation, the whole set of results also fit the experimental data reasonably well. Discrepancies on the absorption and reflection coefficient curves at low frequencies are mainly due to the reflections from the termination of the duct. The distance between the microphones, $L_{\text{mic}} = 80$mm used in the present case, determines the effective frequency range for the measurement, so that more noticeable discrepancies on the absorption or reflection coefficient occur above the frequency $f_{\text{limit}} = c/4L_{\text{mic}} = 1072$Hz. Meanwhile, when approaching the cut-on frequency of the duct, the non-planar nature of the acoustic waves gradually emerges, which may also partly explain the discrepancies at the high frequency end of the curves. Finally, the damping in the system might also be higher than that used in the simulation, the effect of which is more significant at higher frequencies. Nevertheless, we believe the above comparisons can still confirm the validity of the numerical approach. It is relevant to note that by ignoring the pre-processing time needed in FEM like building the geometry model and re-meshing, the proposed method improves the computational efficiency roughly by two orders of magnitude.

4. Numerical results and analyses

4.1. Duct without MPP

The following analyses consider the whole system with rigid walls. In cases where the wall is thin and flexible, its structural vibration will in principle affect the sound absorption of the MPP, which also becomes another design parameter to be considered. Although these effects can definitely be incorporated into the current model, they are not being considered in the present work for simplicity.

As benchmark, the TL of the system without MPP is firstly investigated in Fig. 9. The cut-on frequency of the duct is 1700 Hz. It can be seen that two peaks appear on the TL curve at $f = 1169$Hz and $f = 1625$Hz, respectively, giving rise to high acoustic attenuation within two very narrow bands. These two frequencies are close to the two natural frequencies of the hard-walled trapezoidal cavity: $f_{\text{r}}^{\text{irr}} = 1216$Hz and $f_{\text{r}}^{\text{irr}} = 1608$Hz. To better understand the physical mechanism behind these phenomena, the absorption and reflection coefficient curves are plotted in Fig. 10 by using Eqs. (18) and (20) to separate the absorbed and reflected energy components. It can be seen that the acoustic energy is attenuated nearly entirely by the reflection through typical reactive behavior, as expected, with virtually zero absorption across the entire frequency range. Note the weak absorption observed is due to the damping introduced into the air. The reactive effects are obviously due to the impedance mismatch induced by the cross-sectional changes in the trapezoidal part of the duct. Meanwhile, this also alludes to the necessity of adding absorptions to the system to enhance the acoustic mitigation performance.

For further illustration, the sound pressure distributions inside the duct at these two TL peaks are presented in Fig. 11. It can be clearly seen that the reflections generate standing waves inside the duct with alternating maxima and minima in the sound pressure amplitude along the axial direction, as a result of the interference between the arriving and the reflected waves.

4.2. Effects of the MPP liner

The predicted TL curves with and without MPP are compared in Fig. 12. The parameters of the MPP ($d = t = 0.5$mm and $\delta = 0.954\%$), the partitions and the dimension of the backing cavity are the same as the test sample shown in Fig. 5. It can be seen that the MPP liner generates an additional dominant peak on the TL curve ($f = 979$Hz), increases the TL value and broadens the attenuation bandwidth. Clearly, the acoustic performance of the system is improved after adding the MPP absorber through effective sound absorption.

To further illustrate the above changes brought about by the MPP absorber, the absorption and reflection curves of the system along with the normalized acoustic impedance of the MPP absorber are plotted in Fig. 13. It can be seen that the

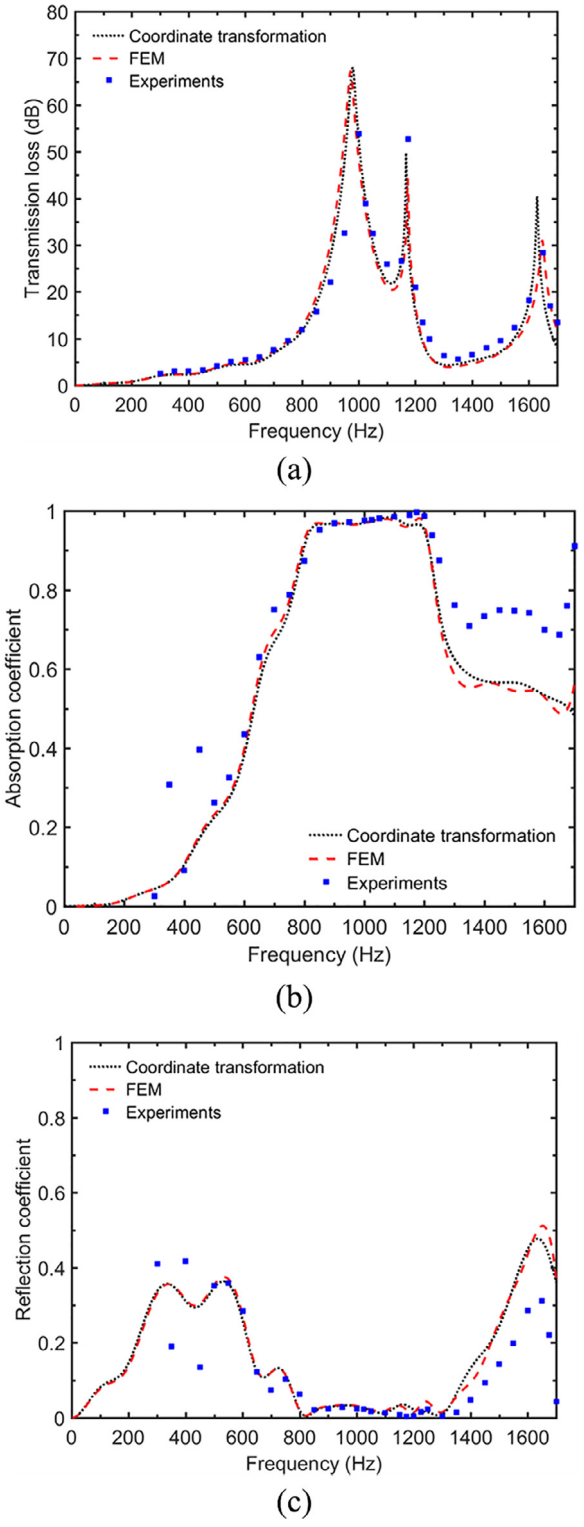

Fig. 8. Comparisons between predictions and the experimental data without flow (a) TL with additional FE results, (b) Sound absorption coefficient, (c) Reflection coefficient.

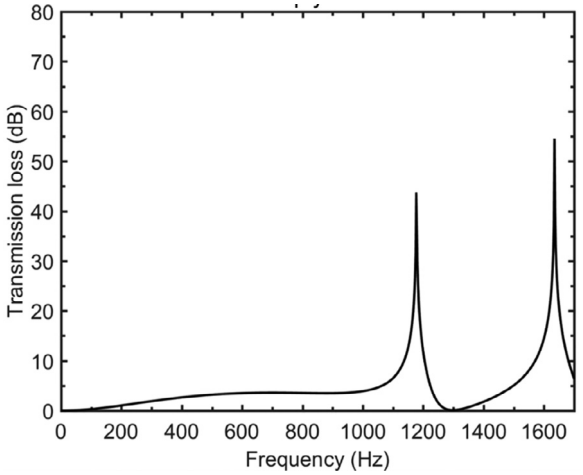

Fig. 9. TL of the model without MPP.

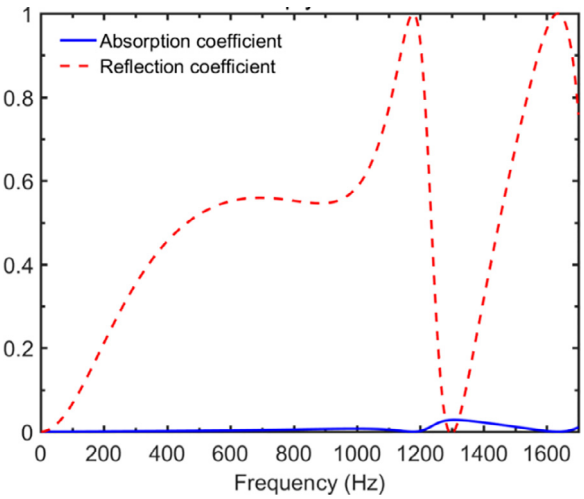

Fig. 10. Sound absorption and reflection coefficient curves without MPP.

location of the absorption peak coincidences with that of the newly appeared TL peak ($f = 979$Hz). Clearly, the new peak is due to the absorption effects of the MPP absorber. The partition inside the backing cavity makes the MPP locally reacting. Consequently, the absorption peak on the absorption curve is induced by the quarter wavelength Helmholtz-type resonance in the backing cavity. Total absorption could be realized at the frequency when perfect impedance match of the acoustic media with that of the MPP takes place. Fig. 13b shows that the normalized reactance is almost zero at $f = 1090$Hz and remains close to zero for in the nearby frequency region. When the MPP liner is coupled to the duct, a high absorption peak is generated when the system undergoes local resonance in the MPP and the backing cavity assembly, thus generating a high sound absorption and a TL peak at $f = 979$Hz. Results in Fig. 13a also indicate that the absorption effects provided by the MPP absorber becomes dominant whilst the reflection effect reduces. To explain this phenomenon, the sound pressure distribution inside the duct at $f = 979$Hz is depicted in Fig. 14. It can be seen that the incoming acoustic wave firstly interacts with the MPP, and then enters into the trapezoidal part of the model and encounters a cross-sectional change, thus entailing wave reflections. The acoustic energy in the lined part decays continuously in the axial direction, thus, within the frequency range where MPP works effectively, most of the energy is absorbed and consequently the energy reflection reduces. However, Fig. 13a also shows that when MPP becomes vulnerable in providing effective absorption, the reflection provided by the system itself can compensate for the deficiency in the energy dissipation of the MPP to ensure a broadband acoustic attenuation. Altogether, such a hybrid mechanism finally ensures a relatively high and broadband TL. Therefore, a good design should be the one which allows for a good balance between the absorption and reflection effects. Of course, it can be expected that, when the absorption effect dominates, MPP absorbers with optimized parameters would warrant even better silencing performance.

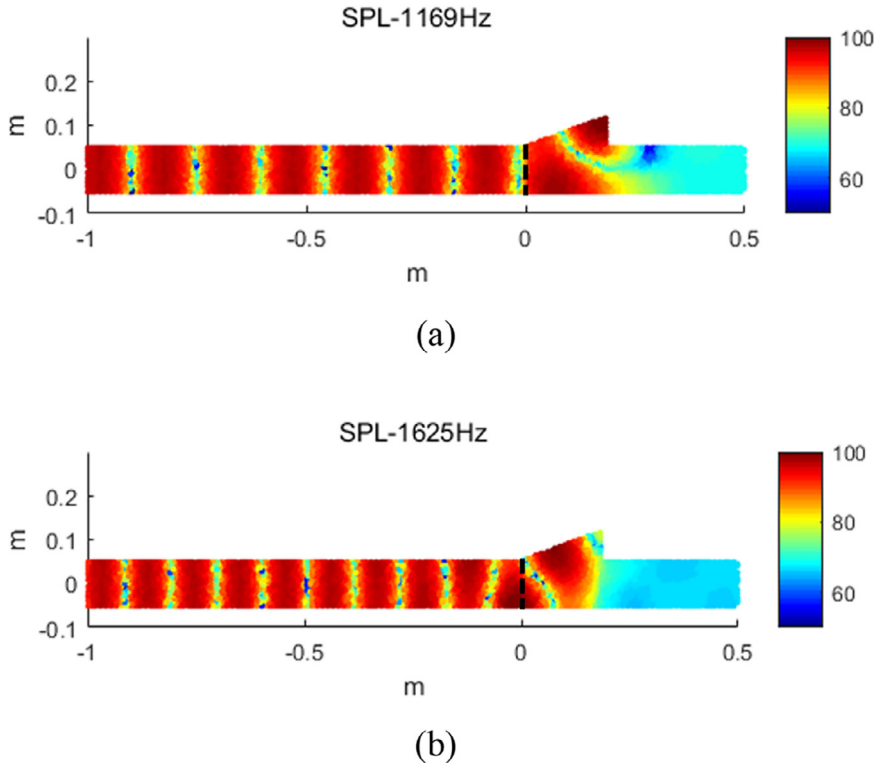

Fig. 11. Sound pressure field inside the duct without MPP. (a) $f = 1169$Hz, (b) $f = 1625$Hz.

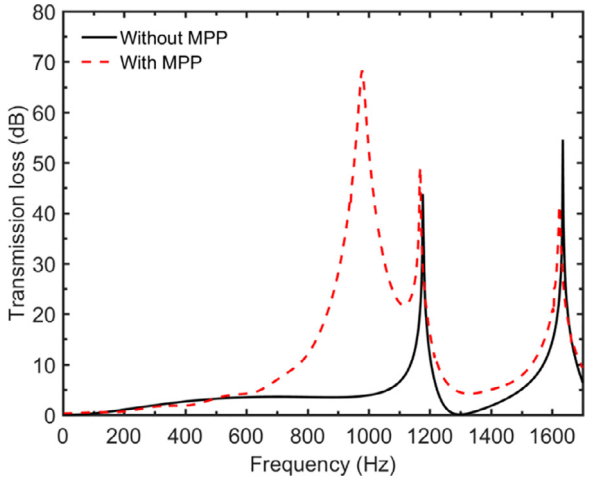

Fig. 12. TL curves of the system with and without MPP.

4.3. Reflective effects through shape changes of the expansion chamber

Aiming at an optimal TL, influences of various system parameters are examined numerically. Since the effects of the MPP-related parameters are relatively well-known [31], analyses mainly focus on the shape of the trapezoidal cavity by capitalizing on the flexibility that is offered by the PTF method, assisted by the coordinate transformation technique on irregular trapezoidal cavities. Analyses intend to demonstrate the necessity to consider the shape of the irregular cavity as an additional parameter to be tuned for an eventual optimal design. As illustrated in Fig. 4, the shape of the trapezoidal cavity is determined by its depth L_{irr} and the inclined angles of the three tilted walls, denoted by α^1_{irr}, α^2_{irr} and β_{irr}, respectively. In the following analyses, the basic geometric configuration of the model remains unchanged and the three tilted walls are assumed to be the same (α^1_{irr}=α^2_{irr}=β_{irr}) for simplicity, which are subject to change alongside the cavity depth L_{irr}.

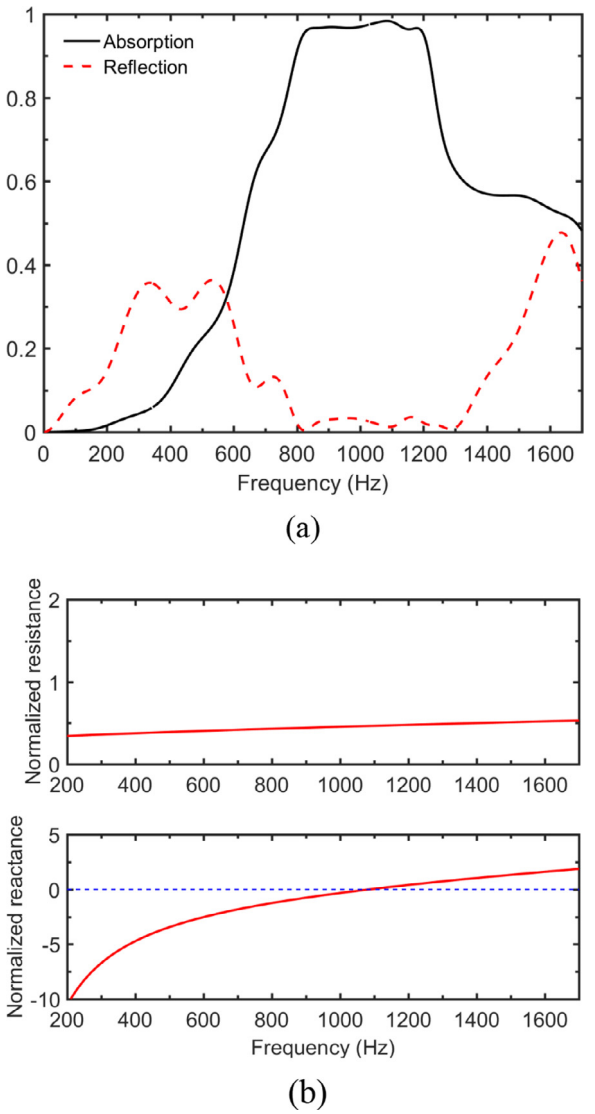

Fig. 13. (a) Sound absorption and reflection coefficient curves of the model with MPP, (b) Normalized acoustic impedance of the MPP absorber.

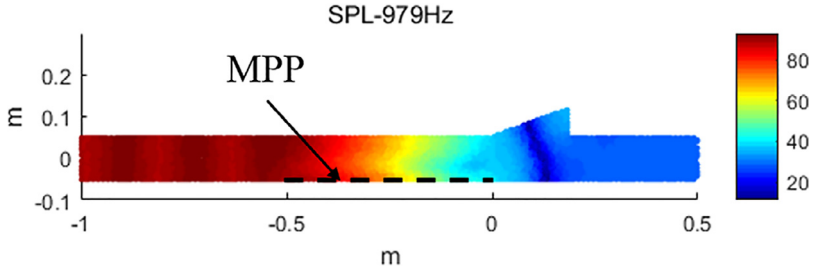

Fig. 14. Sound pressure field in the model with MPP at $f = 979$Hz.

The TL curves of the system with MPP ($d = t = 0.5$mm and $\delta = 1\%$) with different inclined angles of the trapezoidal cavity are compared in Fig. 15. It follows that the tilted angle obviously affects the silencing performance of the system. More specifically, a larger angle increases the number of the peaks on the TL curve, with their locations shifted toward lower frequencies to result in an improvement in the low frequency performance. This is understandable since, except for the peak induced by the absorption effects provided by the MPP absorber at $f = 979$Hz, other peaks are generated by the reflection effects due to the impedance mismatch induced by the cross-sectional changes in the trapezoidal part of the

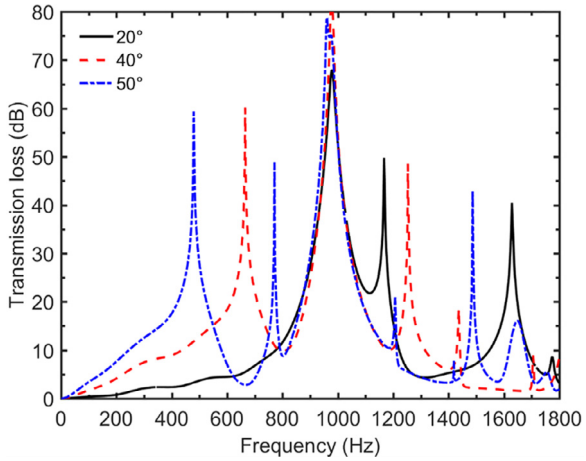

Fig. 15. TL curves of the model having MPP with the trapezoidal cavity having different inclined angles, $d = t = 0.5$mm, and $\delta = 1\%$.

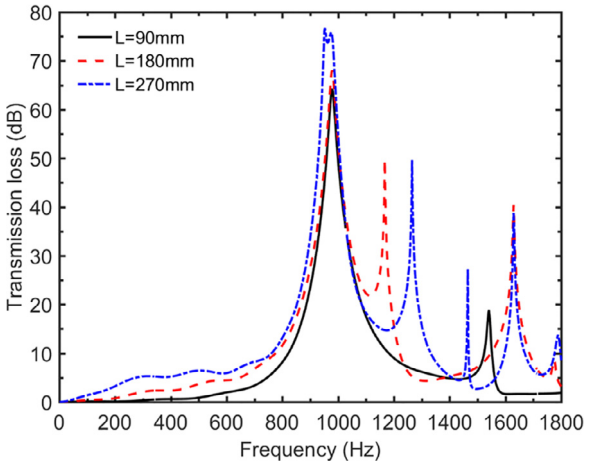

Fig. 16. TL curves of the model with MPP having different irregular cavity depths, $d = t = 0.5$mm, and $\delta = 1\%$.

model. The locations of these peaks roughly correspond to the natural frequencies of the irregular cavity, which decrease in values and increase in numbers when the cavity size increases as the angle of the tilted walls increases.

The influence of the cavity depth, ranging from 90 to 270 mm, is shown in Fig. 16. It follows that cavity depth exerts strongly impact on the TL. As a result of the increasing cavity dimension, similar changes on the TL curves observed from the inclined angles also apply here, such as the enrichment of TL peaks and improvement of TL at lower frequencies.

The above discussions indicate that the TL of the system is sensitive to the shape of the irregular cavity, thus alluding to a possible optimal design through a proper tuning of the cavity geometry. In this case, the computational cost of the conventionally used numerical method such as FEM would be tedious. We will show how the proposed PTF approach can offer a computationally tractable tool for system optimization.

4.4. Optimization study

As an illustrative example, system optimizations are performed through the tuning of two MPP parameters and the shape of the trapezoidal cavity. The perforation ratio δ, the diameter of the hole d, the inclined angles of three tilted walls (set to be the same) and the depth of the trapezoidal cavity, are taken as optimization variables. For a given incident sound power, the averaged transmitted sound power in a prescribed frequency range, $\Pi_{\text{avg}}^{\text{out}}$, is used as the objective function, to evaluate the silencing performance of the system, which is expressed as

$$\prod\nolimits_{\text{avg}}^{\text{out}}(\mathrm{d}, \delta, L_{\text{irr}}, \beta_{\text{irr}}) = \frac{1}{f_u - f_l}\int_{f_l}^{f_u}\prod^{\text{out}}(f)df = \frac{1}{f_u - f_l}\sum_{i=1}^{N_f}\Pi_i^{\text{out}}\Delta f, \tag{25}$$

where f_l and f_u are the lower and upper bounds of the target frequency range, respectively; N_f is the number of discrete and equally spaced frequency points within the frequency range used for calculation and Π_i^{out} is the transmitted sound power

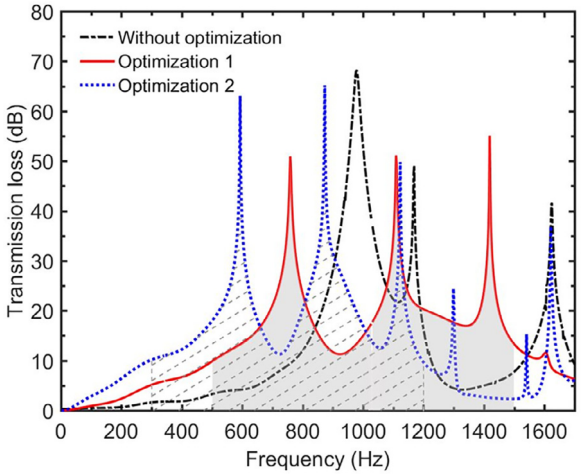

Fig. 17. TL curves of systems with and without optimization.

at one discrete frequency point i in the target frequency range. The optimization is to determine the optimal combination of the four parameters to warrant minimum averaged transmitted sound power, mathematically defined as:

$$\text{min. } \Pi^{\text{out}}_{\text{avg}}(d, \delta, L_{\text{irr}}, \beta_{\text{irr}}), \tag{26a}$$

$$\text{s.t. } 0.1\ \text{mm} \le d \le 0.9\,\text{mm},\ \Delta d = 0.5\,\text{mm}, \tag{26b}$$

$$0.6\% \le \delta \le 2\%,\ \Delta\delta = 0.1\%, \tag{26c}$$

$$0.12\,\text{m} \le L_{\text{irr}} \le 0.24\,\text{m},\ \Delta L_{\text{irr}} = 0.03\,\text{m}, \tag{26d}$$

$$20^\circ \le \beta_{\text{irr}} = \alpha^1_{\text{irr}} = \alpha^2_{\text{irr}} \le 60^\circ,\ \Delta\beta_{\text{irr}} = 10^\circ. \tag{26e}$$

where min. is the abbreviation of *minimize* and s.t. is the abbreviation of *subject to*. The constraints in Eqs. 26(b)–(e) and the corresponding step size used lead to 17 d s, 15 δ s, 5L_{irr}s and 5β_{irr}s. Overall, this results in 6375 different combinations of d, δ, L_{irr} and β_{irr}. Eqs. 26(b)–(e) define the design space used in the optimization. The variation ranges for the hole diameter and perforation ratio are defined according to the common practice adopted in most MPP configurations used in the literature, namely in the submillimeter range for the former and around 1% for the latter. The design space for the inclined angles of the three tilted walls and the depth of the trapezoidal cavity is defined with due consideration to the compactness, feasibility and possible acceptance of the system.

An exhaustive search for all possible combinations under the constraints described by Eqs. 26(b)–(e) is performed to find the best-possible TL. Two optimized problems are defined. The first case considers a broadband optimization problem, targeting a frequency range from 500 to 1500 Hz, discretized by every 10 Hz. This results in a total 100 calculation points within the frequency range. Owing to the sub-structuring treatment of the proposed model, only the PTFs of those sub-systems being changed need to be recalculated in each optimization loop, namely the mobility matrix of the MPP $\mathbf{Y}$ and the PTFs of the irregular trapezoidal cavity $\mathbf{Z}^{\mathbf{SC}}$ in Eq. (14) in the present case. This results in a significant reduction of the calculation cost, which takes less than 6 hours in total using a standard personal computer. This further demonstrates the efficiency of the improved PTF approach for the modelling of such complex systems.

The optimization process finally yields the following optimal combination: $d = 0.2$mm, $\delta = 0.7\%$, $L_{\text{irr}} = 0.15$m and $\beta_{\text{irr}} = 40^\circ$. The corresponding TL curves along with its non-optimized counterpart (used in the previous analysis) are compared in Fig. 17. The comparison shows that the optimized configuration warrants improved TL in the targeted frequency range and exhibits broadband TL characteristics compared with the one without optimization. Compared with its non-optimized counterpart, the optimized duct increases the averaged transmission loss by roughly 3.3 dB within the board frequency range, whilst the non-optimizes one only offers high TL within a few narrow frequency ranges. By varying one design parameter while fixing the other three, the sensitivity of the total transmitted sound power Π^{out} from 500 to 1500 Hz to the variation of design parameters is shown in Fig. 18. It follows that TL is more sensitive to the MPP hole diameter in the present frequency range.

As second example, the targeted frequency range is set from 300 to 1200 Hz, thus targeting a lower frequency band. The optimization process finally results in an optimal combination with $d = 0.4$mm, $\delta = 0.6\%$, $L_{\text{irr}} = 0.21$m and $\beta_{\text{irr}} = 40^\circ$.

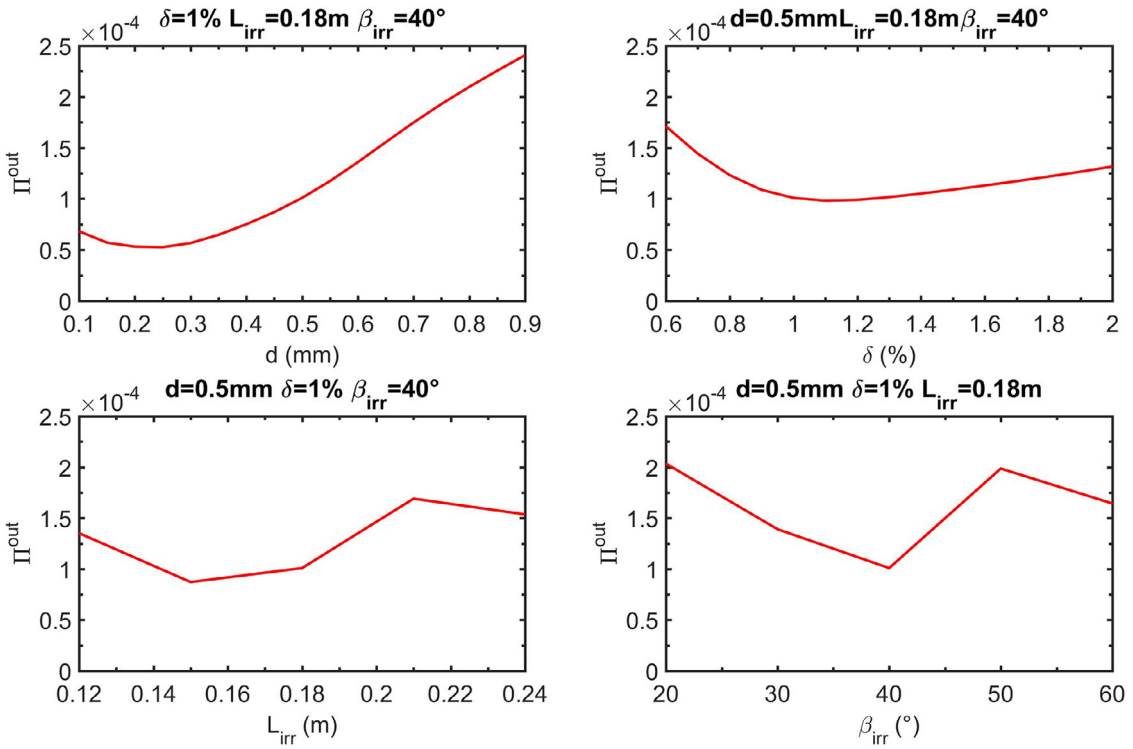

Fig. 18. Total transmitted sound power versus MPP hole diameter d, perforation ratio δ, cavity depth L_{irr} and inclined angles of tilted walls β_{irr} for the first optimization case.

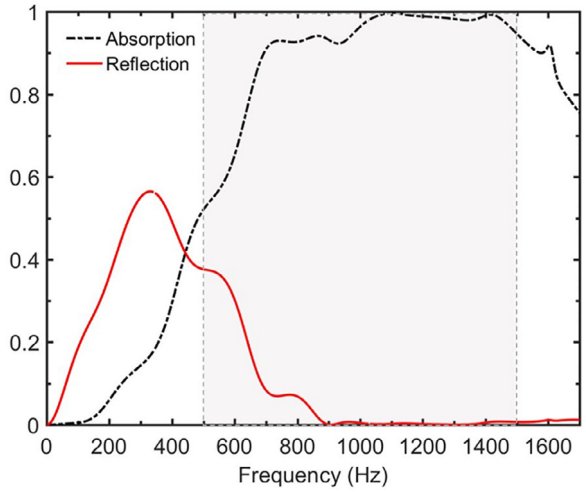

Fig. 19. Sound absorption and reflection coefficient curves for the first optimization case.

Indeed, the corresponding TL curve, plotted in Fig. 17, confirms that the TL of the optimized system is improved in the targeted frequency range by the optimized combination.

To get further insights into the optimization results, the absorption and reflection curves for both cases are plotted in Figs. 19 and 20, respectively. Fig. 19 indicates that the optimized silencing performance from 500 to 1500 Hz in case 1 is achieved by simultaneous absorption and reflection effects. Above 900 Hz, absorption dominates, while below it the absorption effect decreases while the reflection effect increases accordingly to provide compensation. This can be explained by the fact that the bandwidth of the absorption provided by the MPP is not wide enough to cover the entire targeted frequency range. Therefore, reflections are needed. Similar observations can also be made from the comparisons made on case 2 in Fig. 20. Overall, both cases result in a balanced hybrid effect in the system through optimization.

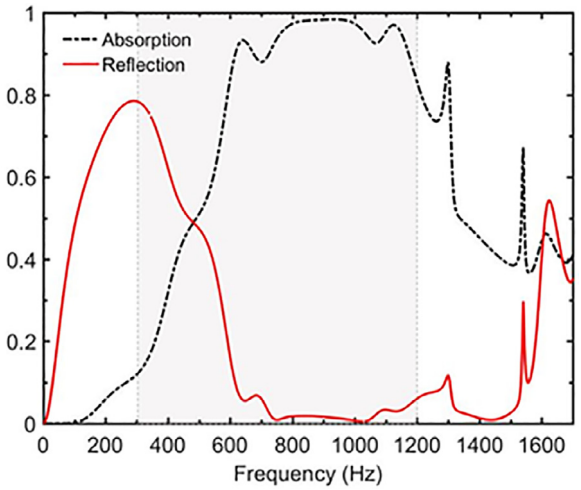

Fig. 20. Sound absorption and reflection coefficient curves for the second optimization case.

The above discussions show that, through embedding the coordinate transformation technique into PTF approach framework, the capability of the PTF approach is significantly enhanced, especially in terms of dealing with irregular system geometrical changes. It can then be used as a practical design and optimization tool for the design of complex systems. Through system mapping, cavities with more general irregular shape can be dealt with. As a result, the proposed improved PTF approach actually can now be applied to even more general cases, not limited to the trapezoidal cavity investigated in the current work.

5. Conclusions

In this paper, an effective modeling technique based on coordinate transformation is established to deal with irregular-shaped acoustic components before its embodiment into a general sub-structuring modelling framework. As a typical application example, the design and optimization of a duct with a Micro-perforated panel (MPP) liner and an irregular-shaped expansion chambers is investigated in views of potential noise control applications.

The coordinate transformation technique is packaged as a subsystem module under the framework of sub-structuring method to improve its capability in modelling vibro/acoustic complex systems which involve irregular-shaped cavity. Experiments conducted in an acoustic duct validate the numerical model and the accuracy of the calculations. With the MPP liner and the expansion chamber, numerical results show a hybrid absorptive-reflective sound attenuation mechanism. Upon ensuring a proper balance between these two effects through parameter tuning, a broadband silencing performance can be achieved. It is further shown that the silencing performance of the system is sensitive to the system parameters including the shape of the expansion chamber. To meet specific TL requirements, system optimization is needed and definitely possible, as illustrated by two optimization examples. Results demonstrate that optimal performance can be achieved within prescribed frequency range through maximizing the aforementioned hybrid noise reduction mechanisms. Results also show the efficacy of the presented modelling technique, in terms of flexibility and computational efficiency, and its potential for practical design of complex systems involving irregular shaped cavity.

Declaration of Competing Interest

The authors declare that they have no known competing financial interests or personal relationships that could have appeared to influence the work reported in this paper.

CRediT authorship contribution statement

Xiaoqi Zhang: Conceptualization, Investigation, Methodology, Validation, Writing - original draft. **Li Cheng:** Conceptualization, Funding acquisition, Project administration, Supervision, Writing - review & editing. **Yang Liu:** Methodology, Writing - review & editing. **Jingtao Du:** Writing - review & editing.

Acknowledgements

The authors thank the support from Research Grant Council of the Hong Kong SAR (PolyU 152036/18E).

References

[1] D.Y. Maa, Theory and design of microperforated panel sound-absorbing constructions, Sci. Sin. 18 (1975) 55–71.
[2] D.Y. Maa, Potential of microperforated panel absorber, J. Acoust. Soc. Am. 104 (1998) 2861–2866.
[3] H. Fuchs, X. Zha, Acrylic-glass sound absorbers in the plenum of the Deutscher Bundestag, Appl. Acoust. 51 (1997) 211–217.
[4] J. Kang, H.V. Fuchs, Predicting the absorption of open wave textiles and micro-perforated membranes backed by an air space, J. Sound Vib. 220 (1999) 905–920.
[5] J. Kang, M. Brocklesby, Feasibility of applying micro-perforated absorbers in acoustic window systems, Appl. Acoust. 66 (2005) 669–689.
[6] W.Z. Yu, Design and noise reduction of elevated road barrier of micro-perforated panels with linear-change cavity, Environ. Pollut. Control 7 (2008) 67–69.
[7] F. Asdrubali, G. Pispola, Properties of transparent sound-absorbing panels for use in noise barriers, J. Acoust. Soc. Am. 121 (2007) 214–221.
[8] G. Li, C.K. Mechefske, A comprehensive experimental study of micro-perforated panel acoustic absorbers in MRI scanners, Magn. Reson. Mater. Phys, Biol. Med. 23 (2010) 177–185.
[9] L. Maxit, C. Yang, L. Cheng, J.L. Guyader, Modeling of micro-perforated panels in a complex vibro-acoustic environment using patch transfer function approach, J. Acoust. Soc. Am. 131 (2012) 2118–2130.
[10] C. Yang, L. Cheng, Sound absorption of microperforated panels inside compact acoustic enclosures, J. Sound Vib. 360 (2016) 140–155.
[11] X. Yu, F. Cui, L. Cheng, On the acoustic analysis and optimization of ducted ventilation systems using a sub-structuring approach, J. Acoust. Soc. Am. 139 (2016) 279–289.
[12] X. Yu, L. Cheng, X. You, Hybrid silencers with micro-perforated panels and internal partitions, J. Acoust. Soc. Am. 137 (2015) 951–962.
[13] X. Wang, Y. Choy, L. Cheng, Hybrid noise control in a duct using a light micro-perforated plate, J. Acoust. Soc. Am. 132 (2012) 3778–3787.
[14] X. Shi, C.M. Mak, Sound attenuation of a periodic array of micro-perforated tube mufflers, Appl. Acoust. 115 (2017) 15–22.
[15] T. Bravo, C. Maury, C. Pinhède, Optimisation of micro-perforated cylindrical silencers in linear and nonlinear regimes, J. Sound Vib. 363 (2016) 359–379.
[16] M.Q. Wu, Micro-perforated panels for duct silencing, Noise Control Eng. J. 45 (1997) 69–77.
[17] X. Yu, L. Cheng, Duct noise attenuation using reactive silencer with various internal configurations, J. Sound Vib. 335 (2015) 229–244.
[18] M. Ouisse, L. Maxit, C. Cacciolati, J.L. Guyader, Patch transfer functions as a tool to couple linear acoustic problems, J. Vib. Acoust. 127 (2005) 458–466.
[19] J. Missaoui, L. Cheng, A combined integro-modal approach for predicting acoustic properties of irregular-shaped cavities, J. Acoust. Soc. Am. 101 (1997) 3313–3321.
[20] I. Cooper, H. Pollard, Low-frequency resonances in unsymmetrical enclosures, Acta Acust. Acust. 41 (1978) 86–93.
[21] P. Hamery, P. Dupire, M. Bruneau, Acoustic fields in trapezoidal cavities, Acta Acust. Acust. 83 (1997) 13–18.
[22] Y. Li, L. Cheng, Modifications of acoustic modes and coupling due to a leaning wall in a rectangular cavity, J. Acoust. Soc. Am. 116 (2004) 3312–3318.
[23] K. Sum, J. Pan, Geometrical perturbation of an inclined wall on decay times of acoustic modes in a trapezoidal cavity with an impedance surface, J. Acoust. Soc. Am. 120 (2006) 3730–3743.
[24] E. Anyunzoghe, L. Cheng, On the extension of the integro-modal approach, J. Sound Vib. 255 (2002) 399–406.
[25] E. Anyunzoghe, L. Cheng, Improved integro-modal approach with pressure distribution assessment and the used of overlapped cavities, Appl. Acoust. 63 (2002) 1233–1255.
[26] K. Kubomura, A theory of substructure modal synthesis, Trans. ASME, J. Appl. Mech. 49 (1982) 903–909.
[27] M. Ookuma, A. Nagamatsu, Vibration analysis by multiple component mode synthesis method, Bull. JSME 27 (1984) 1288–1293.
[28] J.H. Jeong, J.G. Ih, B.C. Lee, A guideline for using the multi-domain BEM for analyzing the interior acoustic field, J. Comp. Acoust. 11 (2003) 403–424.
[29] S. Kim, M. Brennan, A compact matrix formulation using the impedance and mobility approach for the analysis of structural-acoustic systems, J. Sound Vib. 223 (1999) 97–113.
[30] A. Dijckmans, G. Vermeir, W. Lauriks, Sound transmission through finite lightweight multilayered structures with thin air layers, J. Acoust. Soc. Am. 128 (2010) 3513–3524.
[31] X. Zhang, L. Cheng, Acoustic silencing in a flow duct with micro-perforated panel liners, Appl. Acoust. 167 (2020) 107382.
[32] J. Du, Y. Liu, Y. Wang, G. Wang, Vibro-acoustic analysis of an elastically restrained plate duct silencer backed by irregular acoustical cavity, Appl. Acoust. 138 (2018) 60–71.
[33] M. Munjal, A. Doige, Theory of a two source-location method for direct experimental evaluation of the four-pole parameters of an aeroacoustic element, J. Sound Vib. 141 (1990) 323–333.